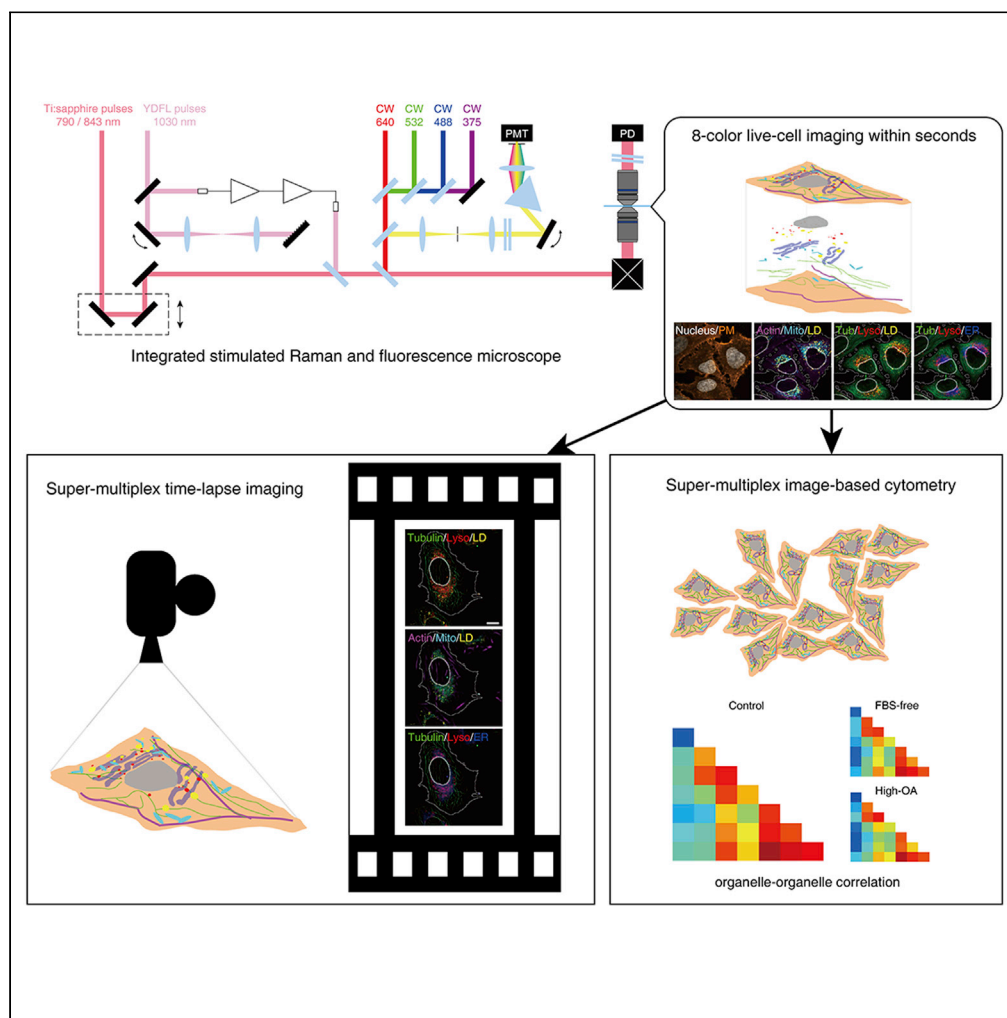## Article

Super-multiplex imaging of cellular dynamics and heterogeneity by integrated stimulated Raman and fluorescence microscopy

Jingwen Shou,
Robert Oda,
Fanghao Hu, ...,
Bruce Shiramizu,
Wei Min, Yasuyuki
Ozeki

hufanghao@tsinghua.edu.cn
(F.H.)
wm2256@columbia.edu
(W.M.)
ozeki@ee.t.u-tokyo.ac.jp (Y.O.)

Highlights

Integrated SRS and
fluorescence microscopy
with fast tunability has
been developed

Eight-color live-cell
imaging can be
conducted with a
temporal resolution of
seconds

Super-multiplex time-
lapse imaging reveals
complex organelle
interactions

Super-multiplex image-
based cytometry accesses
high-dimensional
heterogeneity

iScience

Article

Super-multiplex imaging of cellular dynamics and heterogeneity by integrated stimulated Raman and fluorescence microscopy

Jingwen Shou,[1] Robert Oda,[1,2,3,4] Fanghao Hu,[5,6,*] Keiko Karasawa,[4] Mutsuo Nuriya,[4] Masato Yasui,[4] Bruce Shiramizu,[2,3] Wei Min,[5,7,*] and Yasuyuki Ozeki[1,8,*]

SUMMARY

Observing multiple molecular species simultaneously with high spatiotemporal resolution is crucial for comprehensive understanding of complex, dynamic, and heterogeneous biological systems. The recently reported super-multiplex optical imaging breaks the "color barrier" of fluorescence to achieve multiplexing number over six in living systems, while its temporal resolution is limited to several minutes mainly by slow color tuning. Herein, we report integrated stimulated Raman and fluorescence microscopy with simultaneous multimodal color tunability at high speed, enabling super-multiplex imaging covering diverse molecular contrasts with temporal resolution of seconds. We highlight this technique by demonstrating super-multiplex time-lapse imaging and image-based cytometry of live cells to investigate the dynamics and cellular heterogeneity of eight intracellular components simultaneously. Our technique provides a powerful tool to elucidate spatiotemporal organization and interactions in biological systems.

INTRODUCTION

The ability to simultaneously visualize a large number of distinctive molecular species with high spatiotemporal resolution is crucial for interrogating complex, dynamic, and heterogeneous biological systems but still remains challenging. Recent techniques such as cyclic immunofluorescence (Lin et al., 2015), multiplexed ion beam imaging (Angelo et al., 2014), and imaging mass cytometry (Giesen et al., 2014) provide microscopic images with multiplexed contrasts, while they are all incompatible with living systems, yielding no information in the time domain. Live-cell fluorescence imaging permits the visualization of dynamic biological processes (Valm et al., 2017; Guo et al., 2018), but the number of resolvable colors is limited because of the intrinsically broad (FWHM $\sim$500 cm^{-1}) and featureless fluorescence spectra (Lakowicz, 2013). Indeed, no more than six colors can be distinguished in live cells at subcellular resolution even with sophisticated spectral unmixing (Valm et al., 2017). In addition to being limited by such a "color barrier", it is difficult to image small biomolecules with fluorescence because their physiological properties can be altered by attaching bulky fluorescent probes (Hu et al., 2019). As another powerful optical modality compatible with living systems, Raman imaging can provide additional resolvable colors taking advantage of much narrower spectral linewidth (FWHM $\sim$10 cm^{-1}) by probing the vibrations of chemical bonds (Hu et al., 2019; Min et al., 2011; Cheng and Xie, 2015). More importantly, Raman microscopy can offer complementary imaging contrasts to fluorescence including label-free biochemical compositions (Freudiger et al., 2008; Camp and Cicerone, 2015; Ozeki et al., 2012; Ji et al., 2013; Chen et al., 2020; Sarri et al., 2019), alkyne or isotope tagged small biomolecules (Shen et al., 2019; Azemtsop Matanfack et al., 2020) and the recently developed multiplexed vibrational probes (Wei et al., 2017; Hu et al., 2018).

Hence it will be highly desirable if Raman and fluorescence can be seamlessly integrated. Toward this goal, there are several different Raman candidates such as spontaneous Raman, coherent anti-Stokes Raman scattering (CARS) and surface-enhanced Raman scattering (Hu et al., 2019; Min et al., 2011; Camp and Cicerone, 2015). Among them, stimulated Raman scattering (SRS), which provides vibrational contrasts through detecting the modulation transfer between two-color light fields, is advantageous of high-speed imaging and is immune to non-resonant background and crosstalk from fluorescence emission (Hu et al., 2019; Min et al., 2011; Cheng and Xie, 2015; Freudiger et al., 2008; Camp and Cicerone, 2015; Ozeki et al., 2012; Prince et al., 2016; Ozeki et al., 2019; Liao et al., 2015a, 2015b, 2016). Therefore, our strategy is to integrate the

[1]Department of Electrical Engineering and Information Systems, The University of Tokyo, Tokyo 113-8656, Japan

[2]Department of Molecular Biosciences and Bioengineering, The University of Hawaii, Manoa, 1955 East West Road, Honolulu, Hawaii 96822, USA

[3]Department of Tropical Medicine, Medical Microbiology and Pharmacology, John A. Burns School of Medicine, 651 Ilalo Street, Honolulu, Hawaii 96813, USA

[4]Department of Pharmacology School of Medicine, Keio University, Tokyo 160-8582, Japan

[5]Department of Chemistry, Columbia University, New York, New York 10027, USA

[6]Department of Chemistry, Tsinghua University, Beijing 100084, China

[7]Kavli Institute for Brain Science, Columbia University, New York, New York 10027, USA

[8]Lead contact

*Correspondence: hufanghao@tsinghua.edu.cn (F.H.), wm2256@columbia.edu (W.M.), ozeki@ee.t.u-tokyo.ac.jp (Y.O.)

https://doi.org/10.1016/j.isci.2021.102832

complementary vibrational contrasts of SRS on top of the well-established molecular contrasts of fluorescence to conduct super-multiplex imaging covering a wide variety of cellular targets with high spatiotemporal resolution. However, the currently reported multicolor SRS/fluorescence systems (Wei et al., 2017; Hu et al., 2018) suffer from low time resolution. The main limiting factor of the slow speed is the time cost at color tuning including the modality switching of SRS/fluorescence and the wavelength tuning of excitation or detection for either mode. As a result, a set of super-multiplex images typically takes several minutes (e.g. 10-color live-cell organelle imaging required ~10 min (Hu et al., 2018)), which is unsatisfactory for investigating cellular dynamics or heterogeneity.

Herein, we report an integrated SRS/fluorescence microscope system with simultaneous multimodal color tunability at high speed to conduct super-multiplex imaging of intracellular dynamics and cellular heterogeneity. The rapid color tuning of the developed imaging platform enables us to acquire highly multiplexed images in seconds, over 20 times faster than previous report. On this basis, we demonstrate super-multiplex time-lapse imaging and super-multiplex image-based cytometry of live cells. The high spatiotemporal resolution and diverse multiplexed contrasts supported by two optical modalities render this technique as a powerful tool to investigate the organization and interactions of multiple components in complex and heterogeneous living systems.

RESULTS

Integrated stimulated Raman and fluorescence microscopy enables fast super-multiplex imaging

We developed an integrated SRS (Ozeki et al., 2012; Ozeki et al., 2019) and confocal fluorescence microscope system with high-speed frame-by-frame color tunability, accessing multicolor contrasts from two different modalities in parallel (Figure 1A). Instead of the previously reported successive multicolor SRS and fluorescence acquisition (Wei et al., 2017; Hu et al., 2018), we apply simultaneous SRS/fluorescence excitation and detection, which allows doubled acquisition speed and omits modality switching. Specifically, the pump pulses and Stokes pulses for SRS process are provided respectively by a Ti:sapphire laser (Coherent, Mira900D) working at 76-MHz repetition rate and a home-made ytterbium-doped fiber laser system working at 38-MHz repetition rate, which is half of the former for introducing sub-harmonic intensity modulation. The two-color narrowband picosecond pulses from these near-infrared laser sources excite specific molecular vibrational modes efficiently with high spectral resolution (~5 cm^{-1}) when the wavenumber difference of the two-color pulses matches with the wavenumber of certain vibrational modes. Compared to femtosecond pulses, picosecond pulses alleviate concurrent two-photon fluorescence excitation, which can cause unwanted crosstalk between two modalities and excess photobleaching. Continuous-wave (CW) light from four UV or visible lasers excites one-photon fluorescence. All the laser beams are combined spatially and led to a point-scanning microscope with broadband transmittance and low chromatic aberration by using optimized optical components. The pump pulses and Stokes pulses for SRS process are temporally aligned by adjusting the time delay line. At sample plane, the laser power is ~33 mW and ~46 mW for the pump and Stokes light of SRS process; the power of CW lasers for fluorescence excitation is ~2-240 μW. A resonant galvanometric scanner and an ordinary galvanometric scanner enable 30 times of x-y scan per second. Each of SRS and fluorescence signal is detected by a single detector, which simplifies the system and saves computing resources. For selective fluorescence excitation, the CW laser lines are independently turned on or off. For fast and programmable wavelength tuning, by changing the angle of the galvanometric scanner (GS1) the Stokes wavelength for SRS effect can be tuned from 1014 nm to 1046 nm, corresponding to a wavenumber range of 300 cm^{-1}; the wavelength of fluorescence detection is controlled by tuning the angle of another galvanometric scanner (GS2), offering a tunable spectral response with a flat top and sharp edges (Figure S1). Thanks to these sophisticated instrument integration, every 1/30 s for each of SRS and fluorescence channels, we can tune the wavelengths within <1 ms and collect a frame of 500 × 500 pixels (~70 ns pixel dwell time). As a result, we can simultaneously acquire SRS images of specific wavenumbers and fluorescence images of specific excitation and detection wavelengths, at 30 frame pair per second (Figure 1B). Thus, the total acquisition time of super-multiplex imaging is no longer limited by the color tuning time. Moreover, compared to the multicolor imaging methods based on a detector array (Valm et al., 2017; Liao et al., 2015a), the flexible tuning of our multimodal imaging system allows for allocating optimal imaging parameters for each channel such as (1) matched wavelengths with the spectra of target molecules, which can be obtained via prior hyperspectral characterization (Figure S2), to optimize the detection efficiency and to balance the signal and crosstalk, and (2) independent average numbers to balance for the signal-to-noise difference between channels.
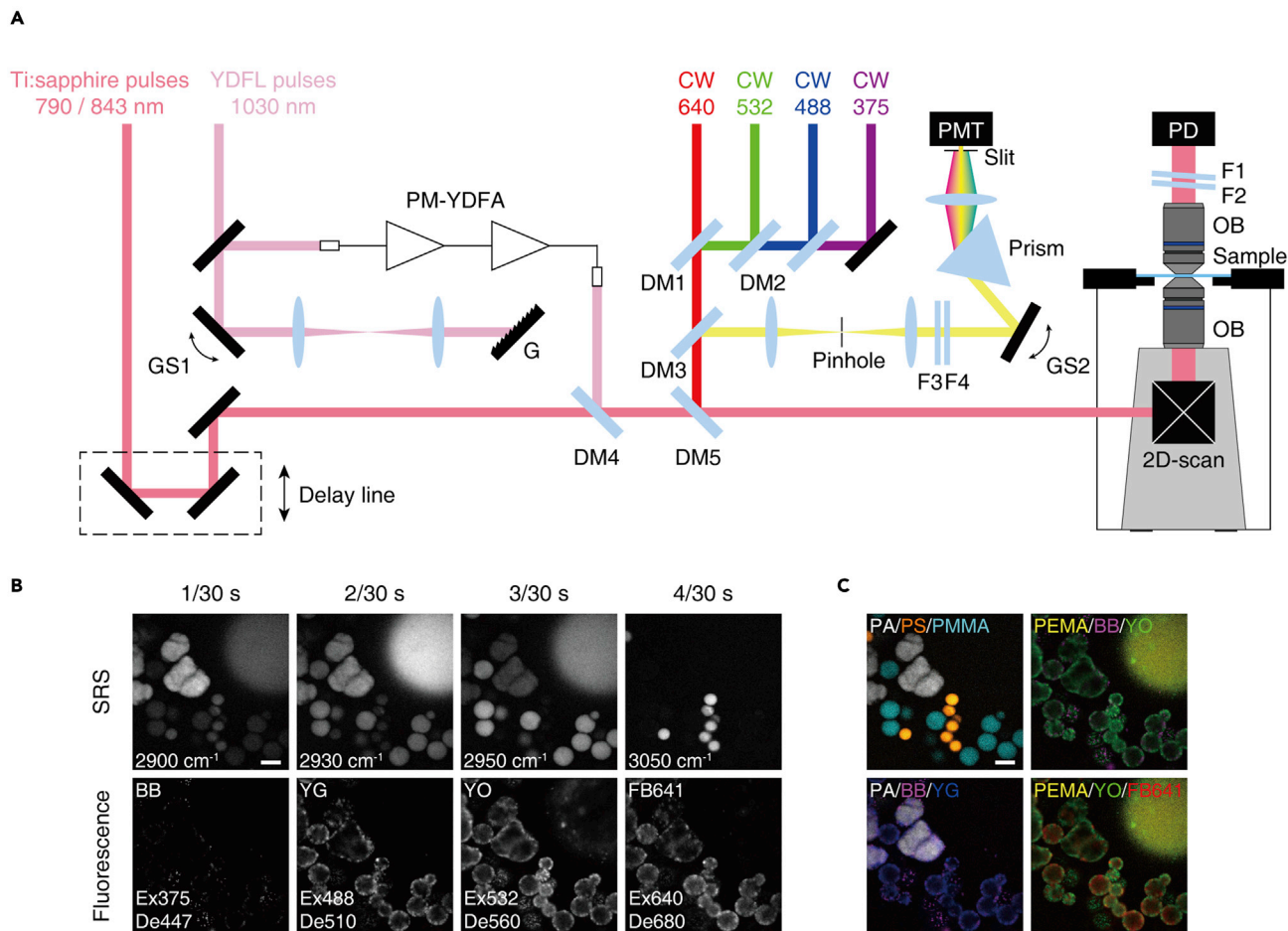
Figure 1. Super-multiplex imaging by integrated stimulated Raman and fluorescence microscopy

(A) Schematic of integrated stimulated Raman and fluorescence microscopy. The wavelength tuning of SRS and fluorescence is achieved by controlling the angles of two galvanometric scanners and the temporal modulation of continuous-wave lasers. YDFL, ytterbium doped fiber laser; CW, continuous-wave laser; PM-YDFA, two-stage polarization-maintaining ytterbium doped fiber amplifier; GS, galvanometric scanner; G, grating; DM, dichroic mirror; OB, objective lens; F, dielectric filter; PD, Si-photodiode; PMT, photomultiplier.

(B) High-speed multicolor SRS and fluorescence imaging of chemical mixture. By specifying different imaging parameters for each frame, eight kinds of contrasts were observed within 133 ms. Ex, excitation wavelength in nm; De: detected central wavelength in nm. (C) Merge of decomposed SRS images and original fluorescence images from raw data in B, representing four kinds of polymers and four kinds of fluorophores. Polymer: PA, polyamide; PEMA, poly(ethyl methacrylate); PMMA, poly(methyl methacrylate); PS, polystyrene. Fluorophore: BB, Bright Blue; YG, Yellow Green; YO, Yellow Orange; FB641, Fluoresbrite 641. Scale bars, 10 μm. (See also Figure S1).

To verify the effectiveness of high-speed frame-by-frame multimodal color tunability, we demonstrate high-speed super-multiplex imaging of chemical mixture (Figures 1B and 1C). The SRS frames at different wavenumbers exhibited characteristic chemical contrasts corresponding to molecular vibrational modes (Figure 1B) and were decomposed to images representing four kinds of polymers, respectively, through linear unmixing (Figure 1C). The fluorescence frames at different excitation and detection wavelengths exhibited the distribution of four fluorophores directly without unmixing (Figures 1B and 1C). By virtue of the seamless integration of SRS and fluorescence microscopy, the 8-color micrographs were acquired within 133 ms, an unprecedented speed for super-multiplex imaging.

Super-multiplex biological imaging visualizes diverse molecular contrasts within seconds

We then demonstrate the versatility of the integrated SRS and fluorescence microscopy to image a wide range of biological species, including intrinsic biomolecules, small metabolites, and specific organelles, as well as cellular markers, in live cells and animal tissues with high multiplexing capability and short acquisition time.
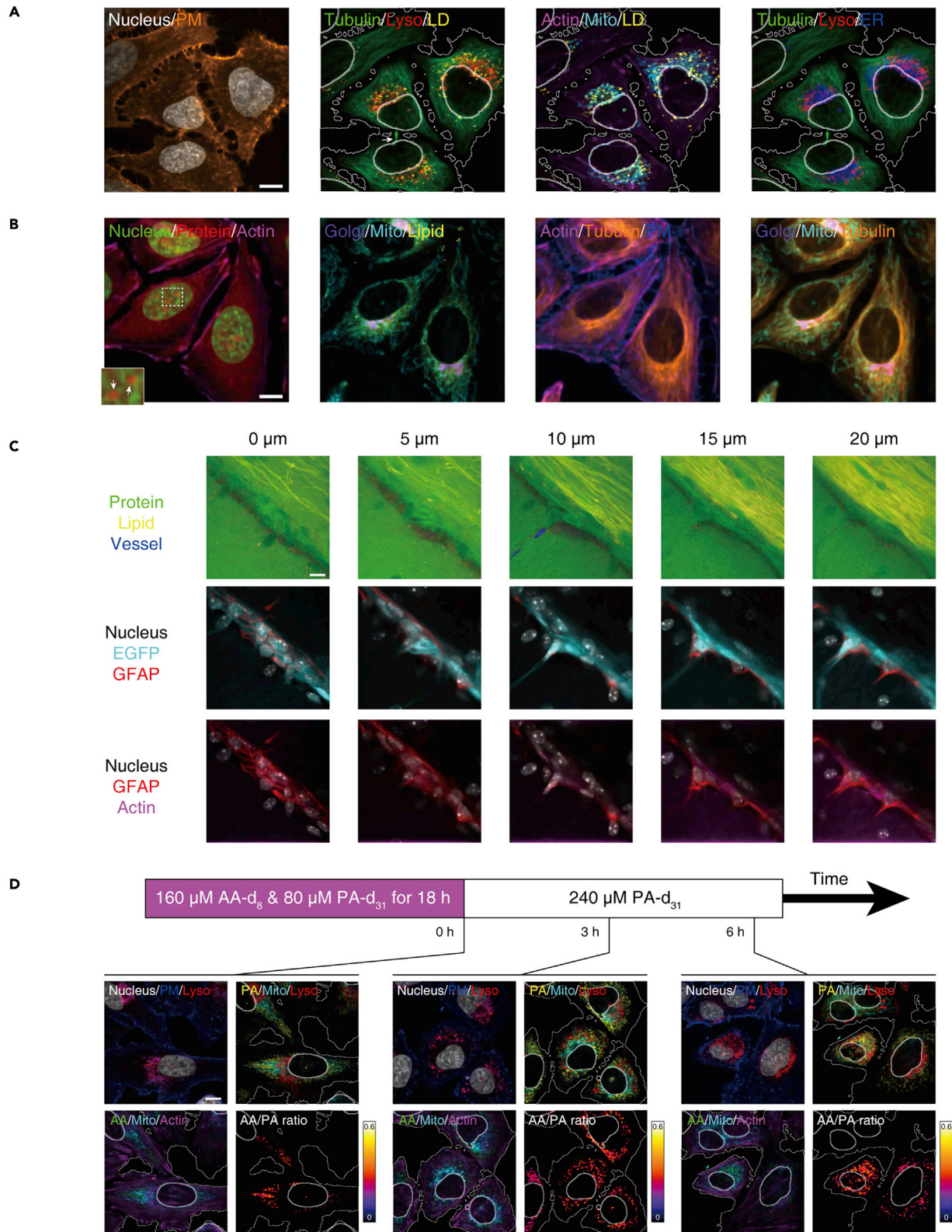
A — Nucleus/PM · Tubulin/Lyso/LD · Actin/Mito/LD · Tubulin/Lyso/ER

B — Nucleus/Protein/Actin · Golgi/Mito/Lipid · Actin/Tubulin/PM · Golgi/Mito/Tubulin

C — 0 μm · 5 μm · 10 μm · 15 μm · 20 μm
Protein/Lipid/Vessel
Nucleus/EGFP/GFAP
Nucleus/GFAP/Actin

D — 160 μM AA-d$_8$ & 80 μM PA-d$_{31}$ for 18 h | 240 μM PA-d$_{31}$ | Time
0 h · 3 h · 6 h
Nucleus/PM/Lyso · PA/Mito/Lyso
AA/Mito/Actin · AA/PA ratio

Figure 2. Super-multiplex imaging of biological specimens covering diverse molecular contrasts

(A) 8-color organelle imaging of live HeLa cells labeled by eight kinds of organelle-targeted Raman and fluorescent probes. SRS: mitochondria (Mito), lysosomes (Lyso), lipid droplets (LD), ER fluorescence: nucleus, plasma membrane (PM), tubulin, actin. The multiplexed images acquired within 30 s display cells undergoing cytokinesis as well as the distribution of all eight kinds of organelles. The arrow indicates the position of midbody.

(B) 8-color imaging of live HeLa cells including label-free SRS imaging. SRS: protein, lipid; fluorescence: nucleus, Mito, PM, Golgi apparatus, tubulin, actin. The total acquisition time was 2 s. Inset shows a magnified view of the area indicated by the dashed box. The arrows indicate the positions of nucleoli.

(C) 7-color depth-resolved imaging of fixed brain tissue slice from CAG-EGFP mouse including label-free SRS imaging. SRS: protein, lipid, blood vessel; fluorescence: nucleus, EGFP driven by a ubiquitous CAG promoter, glial fibrillary acidic protein (GFAP), actin. The acquisition time of seven images at each depth was 16 s, i.e. 80 s for all five depths.

(D) 7-color pulse-chase imaging of live HeLa cells including metabolic imaging. SRS: metabolites of palmitic acid-d_{31} (PA) and arachidonic acid-d_8 (AA); fluorescence: nucleus, Mito, PM, Lyso, actin. The total acquisition time of every seven images was 2 s. The images of AA/PA ratio were calculated from the metabolite images of PA and AA. The contours of nucleus and PM were depicted with solid lines. Scale bars, 10 μm. (See also Figure S2 and S3).

By utilizing organelle-targeted Raman and fluorescent probes (Hu et al., 2018), eight micrographs of live HeLa cells representing different organelle compartments, i.e. mitochondria (Mito), lysosomes (Lyso), lipid droplets (LDs), endoplasmic reticulum (ER) nucleus, plasma membrane (PM), tubulin, and actin, were obtained with an acquisition time of 30 s (Figure 2A). The flexible wavelength tuning with high spectral resolution enables efficient signal acquisition with low crosstalk, and optimal frame averaging to compensate for signal-to-noise differences among different colors (Figures S2 and S3). Also, the crosstalk between fluorescence and SRS imaging is negligible. Compared to one-photon fluorescence, the two-photon fluorescence signals caused by picosecond pulses are much weaker, suggesting that we can neglect the effect of excess photobleaching by two-photon absorption (Figure S2C). And the crosstalk from the concurrent two-photon fluorescence to the one-photon fluorescence channels of other probes is further alleviated by tunable detection. In addition, the negligible spectral overlap among multiple vibrational probes and the utilization of two independent imaging modalities result in a more straightforward post-processing (Figure S3). Therefore, our method can be more tolerant to different brightness of imaging probes and thus more robust for biological applications, compared to the fluorescence spectral unmixing of all channels (Valm et al., 2017), where the relative brightness difference needs to be within ten times for unmixing.

By exploiting the intrinsic carbon-hydrogen vibrations, we can further achieve 8-color imaging of live HeLa cells within 2 s (Figure 2B). From the lipid CH_2 contrast, the position of LDs and inner membranes can be clearly recognized. Inside the nucleus, the protein CH_3 contrast indicates the nucleoli, the site of ribosome biogenesis, while the Hoechst staining shows the distribution of double-stranded DNA. Together with six fluorescence colors, a total of eight kinds of organelles (LD, nucleoli, nucleus, Mito, PM, Golgi apparatus, tubulin, actin) can be recognized simultaneously. Moreover, we applied super-multiplex imaging to mouse brain tissue. 7-color depth-resolved imaging was achieved in fixed brain tissue slice from CAG-EGFP mouse with 16-s acquisition per layer (Figure 2C). In addition to fluorescence contrasts including actin and the astrocyte marker glial fibrillary acidic protein (GFAP), the distribution of proteins, lipid-rich fibers, and blood vessels were visualized by label-free SRS imaging.

Furthermore, by exploiting isotope labeling of small biomolecules, we present 7-color pulse-chase imaging of live HeLa cells with 2-s acquisition to observe the metabolic turnover of saturated and unsaturated fatty acids using deuterated palmitic acid (PA-d_{31}) and arachidonic acid (AA-d_8) (Figure 2D). By calculating the AA/PA ratio, intracellular metabolic heterogeneity can be closely studied along with simultaneous imaging of different kinds of organelles. After removing AA-d_8 from the cell culture media, we found that different cells exhibited distinct AA/PA ratios, which reflect the strong cellular heterogeneity in fatty acid metabolism.

Super-multiplex time-lapse imaging of live cells

To showcase the utility in monitoring the intracellular dynamics of organelle interactome (Valm et al., 2017; Guo et al., 2018), we conducted 8-color time-lapse imaging in live HeLa cells at a temporal resolution of 20 s (Figures 3A and 3B, Video S1), which is more than 24 times faster acquisition speed than before (Hu et al., 2018). We observed the fast movement of PM and the remodeling of tubulin, while the distribution of lysosomes and LDs changed modestly (Video S1). Over the time course of 160 s, the global organelle distribution and the correlation coefficient matrix, which quantifies the colocalization of organelles, maintained a steady state (Figures S4 and S5). In certain area (Figure 3B), LD contacted with tubulin and actin. Mitochondria were shown to distribute around actin, likely to regulate the fusion and fission balance (Moore et al., 2016). More interestingly, the shape of lysosomes changed over time in the proximity of ER, which
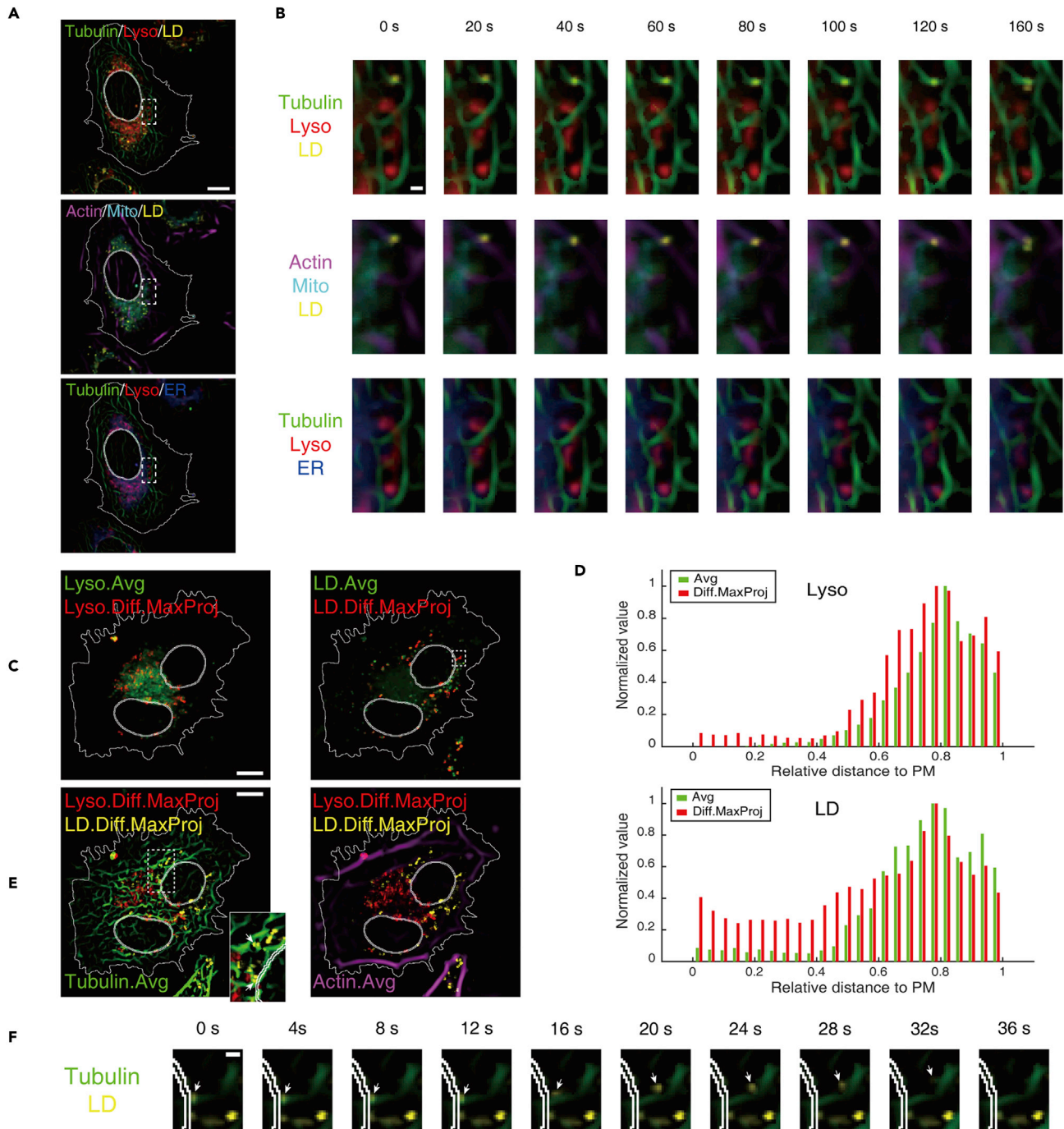
Figure 3. Super-multiplex time-lapse organelle imaging of live cells

(A and B) 8-color time-lapse organelle imaging of live HeLa cells with a temporal resolution of 20 s. (A) Micrographs at the first time point. (B) Time-lapse images in the area indicated by the dashed box in (A).

(C–F) 6-color time-lapse organelle imaging of live HeLa cells with a temporal resolution of 4 s. (C) Comparison of average images and projected difference images of Lyso and LD. (D) Histograms of the normalized sum signal intensity along relative distance to PM, representing distribution analysis of average and projected difference images of Lyso and LD. (E) Simultaneous visualization of projected difference images of Lyso and LD with average images of tubulin and actin. Inset shows a magnified view of the area indicated by the dashed box. The arrows indicate the LDs oscillating in certain directions. (F) Time-lapse images in the area indicated by the dashed box in C show a continuous transport of LD along tubulin in the juxtanuclear region. The arrows indicate the positions of the transported LD. The contours of nucleus and PM were depicted with solid lines. Scale bars, 10 μm (A, C, and E), 1 μm (B and F). (See also Figures S4–S6, Videos S1 and S2).

might be mediated by tubulin during ER-lysosome contact (Raiborg et al., 2015; Pu et al., 2016), implying the significance of multiple organelle coordination. These results suggest that, although the global organelle interactome is conserved, dynamic organelle contacts occur locally across the entire cell (Valm et al., 2017).

Our system also allows us to track the motion of globular organelles (lysosomes, LDs) at a higher speed. We conducted 6-color time-lapse imaging of live HeLa cells at a temporal resolution of 4 s (Figures 3C–3F, Video S2). We observed fast movement of lysosomes and LDs, while the other four organelles showed little change in such a short time (Video S2). To extract the static and dynamic information from the time-lapse stack, we calculated average image and difference images with their maximum intensity projection for each organelle compartment (Figures 3C, 3E, and S6). We then constructed the histograms of the average intensity and projected difference along the relative distance to PM (Figure 3D). The projected difference of lysosomes shows a slightly shifted peak with shorter relative distance to PM compared with the average, suggesting more active movement of lysosomes in the peripheral region. For LDs, combined with tubulin and actin imaging, it is found that some droplets show continuous transport along the tubulin (Figures 3E and 3F), while others show oscillations in the directions that have an angle shift of about 0–45° between the orientation of the tubulin (Figure 3E). These results indicate that tubulin can act as mediators of LD transport, in which LDs are transported by kinesin or dynein along the cytoskeletal filaments (Kilwein and Welte, 2019).

To emphasize the advantage of SRS to observe small metabolites, we conducted 7-color time-lapse imaging of live HeLa cells at a temporal resolution of 2 s (Figure 4, Video S3). Lysosomes and LDs rich in deuterated fatty acids showed more apparent movements than other compartments (Video S3). By extracting the static and dynamic information, we found that the moving LDs appeared more often in the juxtanuclear region and showed higher correlation with lysosomes than that with mitochondria and actin (Figure 4C), which implies the active hydrolysis reaction (Singh et al., 2009). In a certain area near nuclear membrane, we observed the shortening of mitochondria along actin and attaching with lysosomes and LD (Figure 4D), demonstrating complex organelle interactions. In addition to the relatively weaker lysosomes-LD coordination near nucleus (Figure 4D), we also observed in the cytosol that lysosome showed a fast motion and interacts with LD strongly (Figure 4E), demonstrating various ways of organelle interactions. Moreover, we investigated the relationship between AA/PA ratio and different organelles (Figure 4F). The LDs with higher AA/PA ratio were shown to be closer to nucleus (Figures 4B and 4F), which may be related to lipid transport in regulating membrane fluidity gradient (Seu et al., 2006). Compared to other organelles, mitochondria are more correlated with regions of higher AA/PA ratio with a tilted distribution (Figure 4F). This could reflect the different metabolic rate of beta-oxidation for unsaturated and saturated fatty acids depending on the existence of double bonds (Schulz, 1991). Most importantly, these super-multiplex time-lapse images showcase that the rapid multimodal color tuning in our integrated SRS/fluorescence microscopy offers high temporal resolution and efficiently avoids spectral blurring (Figure S7).

Super-multiplex image-based cytometry of live cells

For in-depth analysis of heterogeneous cellular populations, it is crucial to characterize a large number of single cells. Although previous image-based cytometry provides intracellular morphologies at the single-cell level, it suffers from limited number of resolvable colors (Boutros et al., 2015). Here, we demonstrate high-content image-based cytometry of live cells at 2 field of view (FOV)/min with 8 channels in each FOV. 8-color live-cell image-based cytometry can provide rich information of different subcellular structures, which is helpful for high-dimensional single-cell analysis. We investigated the cell-to-cell heterogeneity of live HeLa cells under three different culture conditions (Figures 5 and S8): control medium (control, n = 75); fetal bovine serum (FBS)-free medium (FBS-free, n = 36); and high oleic acid (OA) medium (high-OA, n = 86). To quantify the colocalization of different organelles, the correlation coefficient matrix of organelles inside each single cell was calculated (Figure 5A) and visualized in one t-SNE plot via dimensionality reduction (Figure 5B). The t-SNE plot revealed cellular heterogeneity of different phenotypes. The FBS-free group exhibited a dispersed distribution with large variations, whereas the distribution of control group and high-OA group could be distinguished. Some binary and ternary organelle pairs that globular organelles (lysosomes, LDs) involve in were further statistically analyzed (Figures 5C and 5D). The results reveal the significant statistical difference of organelle interactome in different culture media conditions. The control group generally shows stronger organelle correlations than the FBS-free and high-OA groups. The results may reflect an altered intracellular organelle organization and metabolism in high-OA
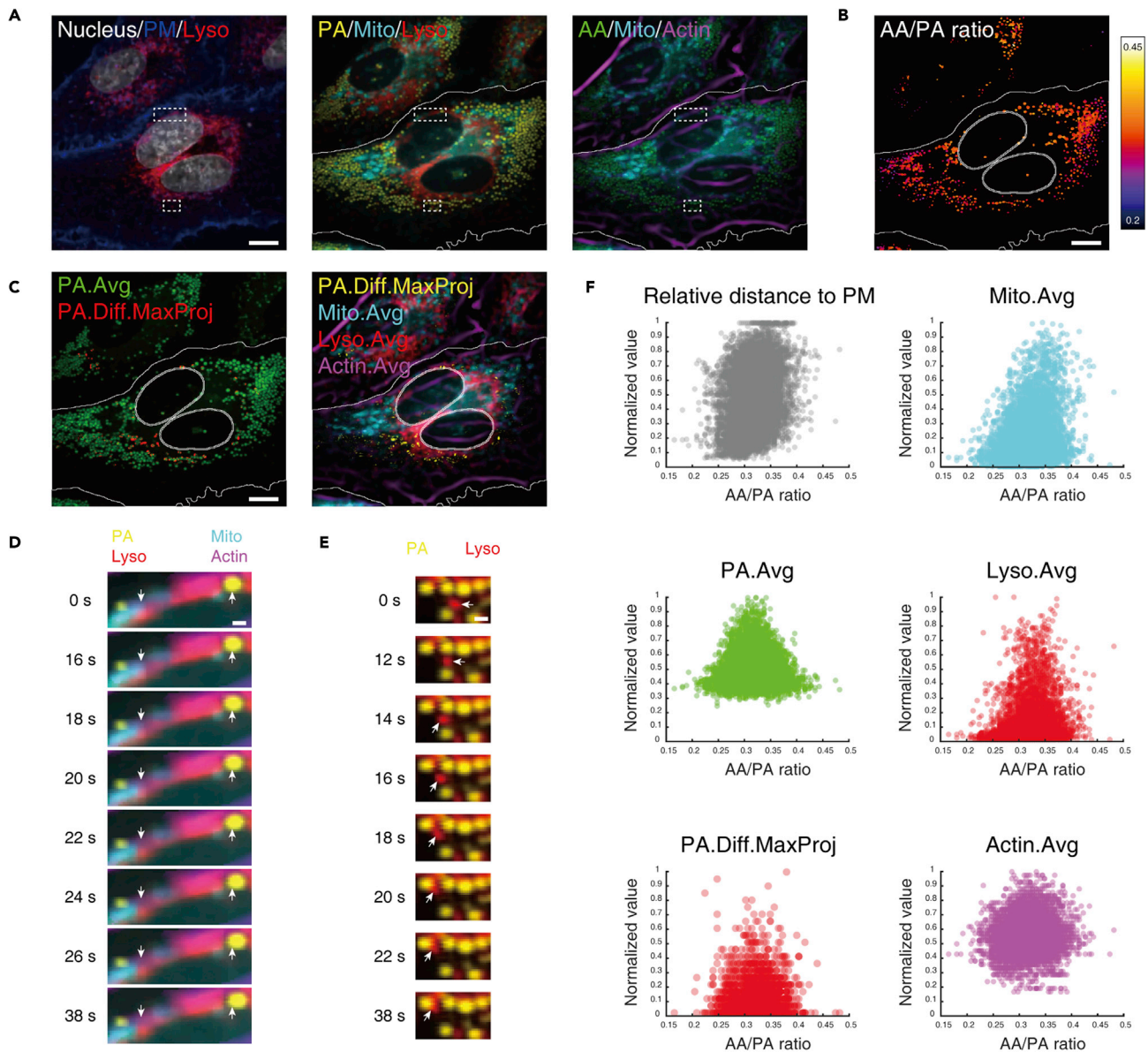
Figure 4. Super-multiplex time-lapse imaging of live cells including metabolite imaging

Seven kinds of molecular contrasts of live HeLa cells were observed with a temporal resolution of 2 s.

(A) Micrographs at the first time point.

(B) The image of AA/PA ratio at the first time point.

(C) Simultaneous visualization of average image and projected difference image of PA metabolites together with average images of Mito, Lyso and actin.

(D) Time-lapse images in the area indicated by the upper dashed box in A showing shortening of Mito along actin and small movement of large LD. The arrows indicate the initial positions of the mitochondria edge and the large LD.

(E) Time lapse images in the area indicated by the lower dashed box in A showing fast motion of lysosome. The arrows indicate the positions of the moving lysosome.

(F) Scatterplots of AA/PA ratio versus relative distance to PM, signal intensity of PA metabolites, Mito, Lyso and actin in the adjacent area. The contours of nucleus and PM were depicted with solid lines. Scale bars, 10 μm (A–C), 1 μm (D and E). (See also Figure S7, Video S3).

environment compared to the control medium, likely to increase fatty acid oxidation (Li et al., 2014). In the FBS-free medium without a lot of growth factors that aid in the cell growth, cells may tend to enter a rested state and become quiescent. This might result in a halting of biological processes, which can cause the low organelle correlations. Importantly, our integrated SRS/fluorescence microscopy can be applied to the
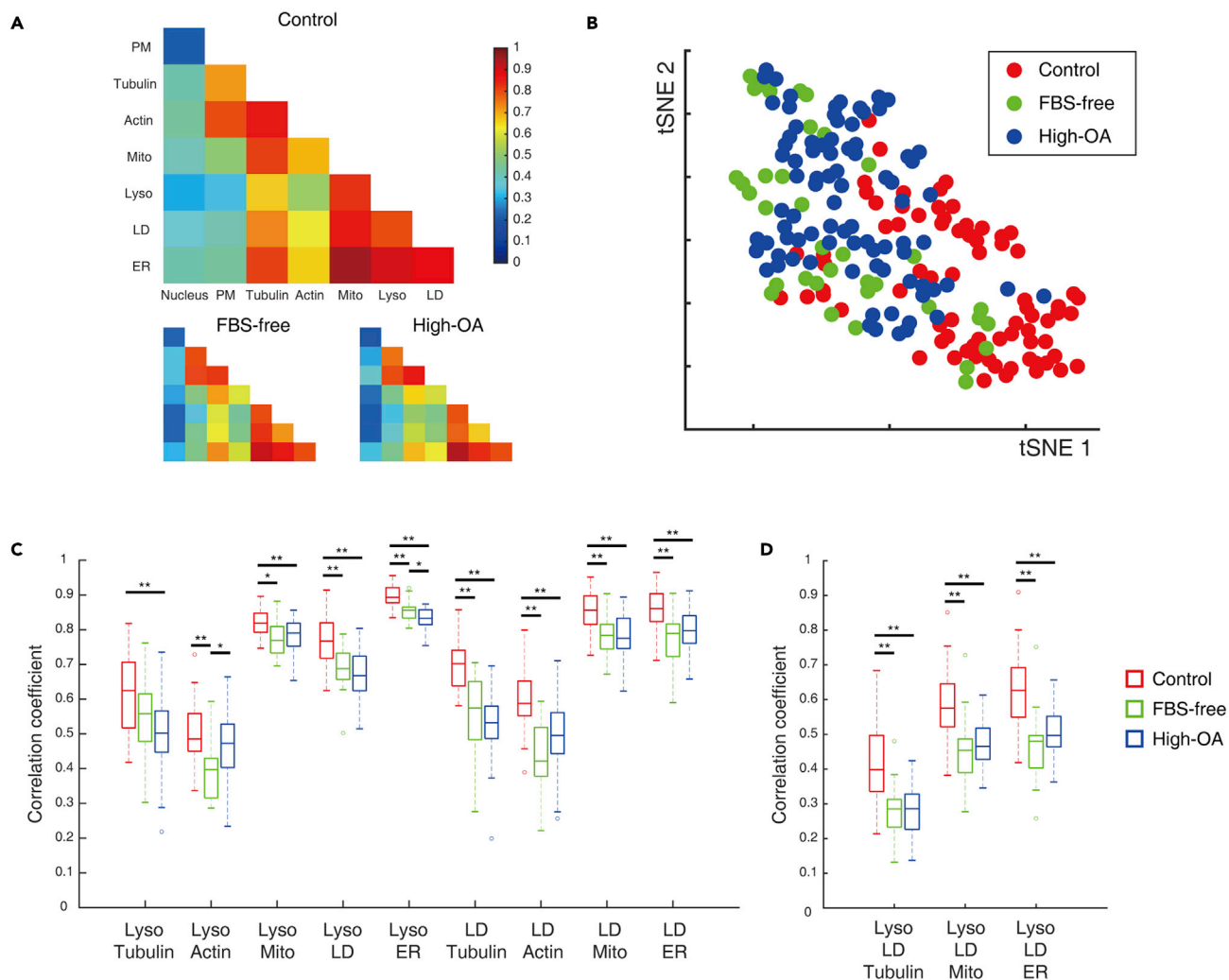
Figure 5. Single-cell analysis of cell-to-cell heterogeneity in organelle interactome by super-multiplex image-based cytometry of live cells
Live HeLa cells grown in different culture conditions, i.e. control medium (control, n = 75), FBS-free medium (FBS-free, n = 36) and high oleic acid medium (high-OA, n = 86), were investigated by 8-color organelle imaging. The throughput was 2 FOV/min.

(A) Matrix representation of medians of organelle correlation coefficients.

(B) t-SNE plot generated from high-dimensional dataset via dimensionality reduction to show cell-to-cell heterogeneity.

(C and D) Box whisker plots of different binary correlation coefficients (C) and ternary correlation coefficients (D). The line in the center of each box represents the median value, the upper and lower edges of the boxes represent the 75th and 25th quantile of the data, and the upper and lower fences represent the furthest observations within the whisker lengths. Observations beyond the whisker lengths are marked as outliers. *p < 0.05, **p < 0.01 (unpaired, two-tailed t test). (See also Figure S8).

super-multiplex imaging of a large number of cells, which allowed us to identify the statistical difference among different groups of heterogeneous populations. The 8-color imaging enables us to interrogate 28 kinds of 2-way organelle interactions as an integration in single-cell heterogeneity analysis. Even though the imaging with 4-5 colors can access all these 28 kinds of 2-way interactions separately by multiple experiments, the results are impeded from single-cell analysis since the connection between different kinds of interactions is not fully preserved for each single cell.

DISCUSSION

The integrated SRS/fluorescence microscopy improved the temporal resolution of super-multiplex live-cell imaging by more than 20 folds from previous minutes level to current seconds level. This platform enabled the super-multiplex time-lapse imaging and image-based cytometry, which provide comprehensive and

high-dimensional data for in-depth analysis of cellular dynamics and heterogeneity. Such high-dimensional data will be useful not only for hypothesis-driven researches but also for discovery-driven ones. Indeed, we found that lysosomes and LDs exhibited different dynamics that are related to diverse intracellular distributions and interactions with other organelles such as tubulin. Also, we revealed specific metabolite-organelle relationships and cellular metabolism heterogeneity at the single-cell level. This technique can be further applied to various cellular conditions, for example, where cells are exposed to different nutrient environments, drug treatments, and pathogen infections, to study their effects on cellular activities such as organelle contacts, intracellular signaling, and transport.

In conclusion, we have reported integrated stimulated Raman and fluorescence microscopy with simultaneous multimodal color tunability at high speed, enabling super-multiplex imaging covering diverse molecular contrasts with temporal resolution of seconds. On this basis, we demonstrated super-multiplex time-lapse imaging and image-based cytometry where up to eight intracellular components were observed simultaneously. The development and functionalization of vibrational color palette (Wei et al., 2017; Hu et al., 2018) and photostable fluorophores can further increase the imaging speed (maximum speed of 17 ms/color), total observation time, and cellular targets (up to 26 colors). We anticipate that the integrated SRS/fluorescence microscopy will be a powerful tool to investigate the dynamics and heterogeneity of complicated living systems and be useful for various biological studies such as intercellular communications, single-cell proteomics, transcriptomics, and the mechanisms of drug actions.

Limitations of the study

The ability of super-multiplex imaging is limited by the available probes and can be further improved with new probe development in the aspect of imaging speed and multiplexing color number. Since our integrated SRS/fluorescence imaging system shortens the color tuning time to just milliseconds, the imaging speed is now limited only by the signal-to-noise ratio. To increase the imaging speed, brighter probes are desired. For example, the Raman signal can be amplified by incorporating alkyne into a polymer backbone (Tian et al., 2020), or loading Carbow into nanoparticles (Zhao et al., 2021). With enhanced signal, it will be possible to conduct super-multiplex imaging in live cells at video rate by our integrated SRS/fluorescence microscopy. Currently, the fast tuning range of 300 cm^{-1} of SRS in our system can afford ~20 colors of vibrational contrasts, which make it possible to resolve up to 26 colors by combining with additional 6 fluorescent colors. Only a few Raman probes in the 20-color vibrational palette (Wei et al., 2017; Hu et al., 2018), however, have been developed for specific labeling in live cells. The efficient functionalization (Hu et al., 2018; Tian et al., 2020; Fujioka et al., 2020) of the entire vibrational palette will be needed to realize the full multiplexing capability for targeted imaging in live cells. Besides, the development of excitation-based spectral fluorescence microscopy is promising to further increase the resolvable color number of fluorescence with low cross talk and at high speed (Chen et al., 2021).

SUPPLEMENTAL INFORMATION

Supplemental information can be found online at https://doi.org/10.1016/j.isci.2021.102832.

STAR★METHODS

Detailed methods are provided in the online version of this paper and include the following:

- KEY RESOURCES TABLE
- RESOURCE AVAILABILITY
  - ○ Lead contact
  - ○ Materials availability
  - ○ Data and code availability
- EXPERIMENTAL MODEL AND SUBJECT DETAILS
  - ○ Cell lines
  - ○ Cell preparation for imaging
  - ○ Tissue preparation for imaging
- METHOD DETAILS
  - ○ Integrated stimulated Raman and fluorescence microscope
  - ○ Chemical mixture
  - ○ Data acquisition and processing

- ○ Calculation of relative distance to PM
- ○ Calculation of correlation coefficient
- ● QUANTIFICATION AND STATISTICAL ANALYSIS

AUTHOR CONTRIBUTIONS

J.S. built the imaging system. F.H. provided Carbow probes. J.S. and F.H. designed the imaging experiments. R.O. worked on the cell culture. J.S., R.O., and F.H. developed and optimized the staining protocol. J.S. and R.O. prepared the cell sample. R.O., K.K., M.N., and M.Y. prepared the tissue sample. J.S. performed imaging experiments and conducted data analysis. Y.O., W.M., and B.S. supervised the research. All authors participated in writing the manuscript.

DECLARATION OF INTERESTS

The authors declare no competing interests.

REFERENCES

Angelo, M., Bendall, S., Finck, R., Hale, M., Hitzman, C., Borowsky, A., Levenson, R., Lowe, J., Liu, S., Zhao, S., et al. (2014). Multiplexed ion beam imaging of human breast tumors. Nat. Med. *20*, 436–442. https://doi.org/10.1038/nm.3488.

Azemtsop Matanfack, G., Rüger, J., Stiebing, C., Schmitt, M., and Popp, J. (2020). Imaging the invisible—bioorthogonal Raman probes for imaging of cells and tissues. J. Biophotonics *13*, e202000129. https://doi.org/10.1002/jbio.202000129.

Boutros, M., Heigwer, F., and Laufer, C. (2015). Microscopy-based high-content screening. Cell *163*, 1314–1325. https://doi.org/10.1016/j.cell.2015.11.007.

Camp, C., Jr., and Cicerone, M. (2015). Chemically sensitive bioimaging with coherent Raman scattering. Nat. Photon. *9*, 295–305. https://doi.org/10.1038/nphoton.2015.60.

Chen, W., Lemieux, G., Camp, C., Chang, T., Ashrafi, K., and Cicerone, M. (2020). Spectroscopic coherent Raman imaging of Caenorhabditis elegans reveals lipid particle diversity. Nat. Chem. Biol. *16*, 1087–1095. https://doi.org/10.1038/s41589-020-0565-2.

Chen, K., Yan, R., Xiang, L., and Xu, K. (2021). Excitation spectral microscopy for highly multiplexed fluorescence imaging and quantitative biosensing. Light Sci. Appl. *10*, 97. https://doi.org/10.1038/s41377-021-00536-3.

Cheng, J., and Xie, X. (2015). Vibrational spectroscopic imaging of living systems: an emerging platform for biology and medicine. Science *350*, aaa8870. https://doi.org/10.1126/science.aaa8870.

Dabov, K., Foi, A., and Egiazarian, K. (2007a). Video denoising by sparse 3D transform-domain collaborative filtering. Proc. Eur. Signal Process. Conf. (Eusipco-2007), 145–149. https://doi.org/10.5281/ZENODO.40233.

Dabov, K., Foi, A., Katkovnik, V., and Egiazarian, K. (2007b). Image denoising by sparse 3-D transform-domain collaborative filtering. IEEE Trans. Image Process. *16*, 2080–2095. https://doi.org/10.1109/TIP.2007.901238.

Freudiger, C., Min, W., Saar, B., Lu, S., Holtom, G., He, C., Tsai, J., Kang, J., and Xie, X. (2008). Label-free biomedical imaging with high sensitivity by stimulated Raman scattering microscopy. Science *322*, 1857–1861. https://doi.org/10.1126/science.1165758.

Fujioka, H., Shou, J., Kojima, R., Urano, Y., Ozeki, Y., and Kamiya, M. (2020). Multicolor activatable Raman probes for simultaneous detection of plural enzyme activities. J. Am. Chem. Soc. *142*, 20701–20707. https://doi.org/10.1021/jacs.0c09200.

Giesen, C., Wang, H., Schapiro, D., Zivanovic, N., Jacobs, A., Hattendorf, B., Schüffler, P., Grolimund, D., Buhmann, J., Brandt, S., et al. (2014). Highly multiplexed imaging of tumor tissues with subcellular resolution by mass cytometry. Nat. Methods *11*, 417–4220. https://doi.org/10.1038/nmeth.2869.

Guo, Y., Li, D., Zhang, S., Yang, Y., Liu, J., Wang, X., Liu, C., Milkie, D., Moore, R., Tulu, U., et al. (2018). Visualizing intracellular organelle and cytoskeletal interactions at nanoscale resolution on millisecond timescales. Cell *175*, 1430–1442. https://doi.org/10.1016/j.cell.2018.09.057.

Hu, F., Zeng, C., Long, R., Miao, Y., Wei, L., Xu, Q., and Min, W. (2018). Supermultiplexed optical imaging and barcoding with engineered polyynes. Nat. Methods *15*, 194–200. https://doi.org/10.1038/nmeth.4578.

Hu, F., Shi, L., and Min, W. (2019). Biological imaging of chemical bonds by stimulated Raman scattering microscopy. Nat. Methods *16*, 830–842. https://doi.org/10.1038/s41592-019-0538-0.

Ji, M., Orringer, D., Freudiger, C., Ramkissoon, S., Liu, X., Lau, D., Golby, A., Norton, I., Hayashi, M., Agar, N., et al. (2013). Rapid, Label-free detection of brain tumors with stimulated Raman scattering microscopy. Sci. Transl. Med. *5*, 201ra119. https://doi.org/10.1126/scitranslmed.3005954.

Kilwein, M., and Welte, M. (2019). Lipid droplet motility and organelle contacts. Contact *2*, 1–13. https://doi.org/10.1177/2515256419895688.

Lakowicz, J. (2013). Principles of Fluorescence Spectroscopy, Third edition (Springer).

Li, S., Zhou, T., Li, C., Dai, Z., Che, D., Yao, Y., Li, L., Ma, J., Yang, X., and Gao, G. (2014). High metastaticgastric and breast cancer cells consume oleic acid in an AMPK dependent manner. PLoS One 9, e97330. https://doi.org/10.1371/journal.pone.0097330.

Liao, C., Slipchenko, M., Wang, P., Li, J., Lee, S., Oglesbee, R., and Cheng, J. (2015a). Microsecond scale vibrational spectroscopic imaging by multiplex stimulated Raman scattering microscopy. Light Sci. Appl. 4, e265. https://doi.org/10.1038/lsa.2015.38.

Liao, C., Wang, P., Wang, P., Li, J., Lee, H., Eakins, G., and Cheng, J. (2015b). Spectrometer-free vibrational imaging by retrieving stimulated Raman signal from highly scattered photons. Sci. Adv. 1, e1500738. https://doi.org/10.1126/sciadv.1500738.

Liao, C., Huang, K., Hong, W., Chen, A., Karanja, C., Wang, P., Eakins, G., and Cheng, J. (2016). Stimulated Raman spectroscopic imaging by microsecond delay-line tuning. Optica 3, 1377. https://doi.org/10.1364/OPTICA.3.001377.

Lin, J., Fallahi-Sichani, M., and Sorger, P. (2015). Highly multiplexed imaging of single cells using a high-throughput cyclic immunofluorescence method. Nat. Commun. 6, 8390. https://doi.org/10.1038/ncomms9390.

Min, W., Freudiger, C., Lu, S., and Xie, X. (2011). Coherent nonlinear optical imaging: beyond fluorescence microscopy. Annu. Rev. Phys. Chem. 62, 507–530. https://doi.org/10.1146/annurev.physchem.012809.103512.

Moore, A., Wong, Y., Simpson, C., and Holzbaur, E. (2016). Dynamic actin cycling through mitochondrial subpopulations locally regulates the fission–fusion balance within mitochondrial networks. Nat. Commun. 7, 12886. https://doi.org/10.1038/ncomms12886.

Ozeki, Y., Umemura, W., Otsuka, Y., Satoh, S., Hashimoto, H., Sumimura, K., Nishizawa, N.,

Fukui, K., and Itoh, K. (2012). High-speed molecular spectral imaging of tissue with stimulated Raman scattering. Nat. Photon. 6, 845–851. https://doi.org/10.1038/nphoton.2012.263.

Ozeki, Y., Asai, T., Shou, J., and Yoshimi, H. (2019). Multicolor stimulated Raman scattering microscopy with fast wavelength-tunable Yb fiber laser. IEEE J. Sel. Top. Quan. Electron. 25, 7100211. https://doi.org/10.1109/JSTQE.2018.2830816.

Prince, R., Frontiera, R., and Potma, E. (2016). Stimulated Raman scattering: from bulk to nano. Chem. Rev. 117, 5070–5094. https://doi.org/10.1021/acs.chemrev.6b00545.

Pu, J., Guardia, C., Keren-Kaplan, T., and Bonifacino, J. (2016). Mechanisms and functions of lysosome positioning. J. Cell Sci. 129, 4329–4339. https://doi.org/10.1242/jcs.196287.

Raiborg, C., Wenzel, E., Pedersen, N., Olsvik, H., Schink, K., Schultz, S., Vietri, M., Nisi, V., Bucci, C., Brech, A., et al. (2015). Repeated ER–endosome contacts promote endosome translocation and neurite outgrowth. Nature 520, 234–238. https://doi.org/10.1038/nature14359.

Sarri, B., Canonge, R., Audier, X., Lavastre, V., Pénarier, G., Alie, J., and Rigneault, H. (2019). Discriminating polymorph distributions in pharmaceutical tablets using stimulated Raman scattering microscopy. J. Raman Spectrosc. 50, 1896–1904. https://doi.org/10.1002/jrs.5743.

Schindelin, J., Arganda-Carreras, I., Frise, E., Kaynig, V., Longair, M., Pietzsch, T., Preibisch, S., Rueden, C., Saalfeld, S., Schmid, B., et al. (2012). Fiji: an open-source platform for biological-image analysis. Nat. Methods 9, 676–682. https://doi.org/10.1038/nmeth.2019.

Schulz, H. (1991). Beta oxidation of fatty acids. Biochim. Biophys. Acta Lipids Lipid Metab. 1081, 109–120. https://doi.org/10.1016/0005-2760(91)90015-A.

Seu, K., Cambrea, L., Everly, R., and Hovis, J. (2006). Influence of lipid chemistry on membrane fluidity: Tail and headgroup interactions. Biophys. J. 91, 3727–3735. https://doi.org/10.1529/biophysj.106.084590.

Shen, Y., Hu, F., and Min, W. (2019). Raman imaging of small biomolecules. Annu. Rev. Biophys. 48, 347–369. https://doi.org/10.1146/annurev-biophys-052118-115500.

Singh, R., Kaushik, S., Wang, Y., Xiang, Y., Novak, I., Komatsu, M., Tanaka, K., Cuervo, A., and Czaja, M. (2009). Autophagy regulates lipid metabolism. Nature 458, 1131–1135. https://doi.org/10.1038/nature07976.

Tian, S., Li, H., Li, Z., Tang, H., Yin, M., Chen, Y., Wang, S., Gao, Y., Yang, X., Meng, F., et al. (2020). Polydiacetylene-based ultrastrong bioorthogonal Raman probes for targeted live-cell Raman imaging. Nat. Commun. 11, 81. https://doi.org/10.1038/s41467-019-13784-0.

Valm, A., Cohen, S., Legant, W., Melunis, J., Hershberg, U., Wait, E., Cohen, A., Davidson, M., Betzig, E., and Lippincott-Schwartz, J. (2017). Applying systems-level spectral imaging and analysis to reveal the organelle interactome. Nature 546, 162–167. https://doi.org/10.1038/nature22369.

Wei, L., Chen, Z., Shi, L., Long, R., Anzalone, A., Zhang, L., Hu, F., Yuste, R., Cornish, V., and Min, W. (2017). Super-multiplex vibrational imaging. Nature 544, 465–470. https://doi.org/10.1038/nature22051.

Zhao, Z., Chen, C., Wei, S., Xiong, H., Hu, F., Miao, Y., Jin, T., and Min, W. (2021). Ultra-bright Raman dots for multiplexed optical imaging. Nat. Commun. 12, 1305. https://doi.org/10.1038/s41467-021-22585-3.

STAR★METHODS

KEY RESOURCES TABLE

REAGENT or RESOURCE	SOURCE	IDENTIFIER
Antibodies		
Anti-glial fibrillary acidic protein conjugated to Cy3	abcam	Abcam Cat# ab49874, RRID:AB_880203
Biological samples		
Fixed brain tissue slice from CAG-EGFP mouse	This paper	N/A
Chemicals, peptides, and recombinant proteins		
Oleic acid	Wako Pure Chemical Industries	155-03401
Arachidonic acid-d8	Cayman Chemical	390010
Palmitic acid-d31	Wako Pure Chemical Industries	16497
Carbow Mito	Hu et al., 2018	N/A
Carbow Lyso	Hu et al., 2018	N/A
Carbow LD	Hu et al., 2018	N/A
Carbow ER	Hu et al., 2018	N/A
NucSpot 488	Biotium	40081-T
Tubulin Tracker Deep Red	Invitrogen	T34077
SiR700-Actin	Cytoskeleton	CY-SC013
WGA Alexa 594	Invitrogen	W11262
BODIPY TR	Invitrogen	B34400
MitoTracker Green	Invitrogen	M7514
NucBlue	Invitrogen	R37605
WGA Alexa 555	Invitrogen	W32464
LysoTracker Deep Red	Invitrogen	L12492
Phalloidin Alexa 647	Invitrogen	A22287
Experimental models: Cell lines		
Human: HeLa cells	RIKEN BRC	0007
Software and algorithms		
Fiji	Schindelin et al., 2012	https://imagej.net/Fiji
MATLAB codes	This paper	N/A
Other		
Polyamide (PA) particles	Sigma-Aldrich	GF71024565-1EA
Poly(ethyl methacrylate) (PEMA) particles	Polysciences	03197-250
Poly(methyl methacrylate) (PMMA) particles	Sekisui	SSX-110
Polystyrene (PS) particles	Polysciences	07312
Bright Blue (BB) microspheres	Polysciences	18339
Yellow Green (YG) microspheres	Polysciences	15700
Yellow Orange (YO) microspheres	Polysciences	18720
Fluoresbrite 641 microspheres	Polysciences	21116

RESOURCE AVAILABILITY

Lead contact

Further information and requests for resources and reagents should be directed to and will be fulfilled by the lead contact, Yasuyuki Ozeki (ozeki@ee.t.u-tokyo.ac.jp).

Materials availability

This study did not generate new unique reagents.

Data and code availability

The data that support the findings of this study are available from the corresponding author upon reasonable request. The code for analysis is available at: https://github.com/JingwenShou/2021-iScience-Shou.

EXPERIMENTAL MODEL AND SUBJECT DETAILS

Cell lines

HeLa cells provided from RIKEN BRC were used for analysis. The cells were cultured in Dulbecco's Modified Eagle Medium (DMEM) (Invitrogen, 12320032) supplemented with 10% fetal bovine serum (FBS) (GE Health Care Biosciences, SH30079.03). All cell cultures were maintained in a humidified environment at 37°C and 5% CO_2.

Cell preparation for imaging

8-color image-based cytometry. Cells were cultured on glass coverslips in a 4-well plate. 6 hours before imaging, the culture media were replaced with DMEM supplemented with 10% FBS and 10 μM oleic acid (Wako Pure Chemical Industries, 155-03401) for control group; FBS-free DMEM supplemented with 10 μM oleic acid for FBS-free group; and DMEM supplemented with 10% FBS and 50 μM oleic acid for high-OA group. 10 μM Carbow LD were added in the culture media for 6 hours at 37°C. 5 μM Carbow Mito, 2 μM Carbow Lyso, 20 μM Carbow ER, 1X NucSpot 488 (Biotium, 40081-T), 1X Tubulin Tracker Deep Red (Invitrogen, T34077), and 1 μM SiR700-Actin (Cytoskeleton, CY-SC013) were added in the culture media for 1 hour at 37°C. Before imaging, cells were labeled with 5 μg/mL WGA Alexa 594 (Invitrogen, W11262) in Hank's buffered salt solution (HBSS) (Invitrogen, 14170120) for 10 min at 37°C. All samples were washed with live cell imaging solution (Invitrogen, A14291DJ) and assembled into a chamber using an imaging spacer filled with live cell imaging solution supplemented with 1% Prolong live antifade reagent (Invitrogen, P36975) for imaging.

8-color time-lapse organelle imaging. Cells were cultured on a glass coverslip in a 4-well plate. 10 μM oleic acid and 10 μM Carbow LD were added in the culture media for overnight at 37°C before imaging. 5 μM Carbow Mito, 2 μM Carbow Lyso, 20 μM Carbow ER, 1X NucSpot 488, 1X Tubulin Tracker Deep Red, 1 μM SiR700-Actin were added in the culture media for 1 hour at 37°C. Before imaging, cells were labeled with 5 μg/mL WGA Alexa 594 in HBSS for 10 min at 37°C. The sample was washed by FluoroBrite DMEM (Invitrogen, A1896701) and assembled into a chamber using an imaging spacer filled with FluoroBrite DMEM supplemented with 1% Prolong live antifade reagent for imaging.

6-color time-lapse organelle imaging. Cells were cultured on a glass coverslip in a 4-well plate. 10 μM oleic acid and 10 μM Carbow LD were added in the culture media for overnight at 37°C before imaging. 2 μM Carbow Lyso, 1X NucSpot 488, 1X Tubulin Tracker Deep Red, 1 μM SiR700-Actin were added in the culture media for 1 hour at 37°C. Before imaging, cells were labeled with 5 μg/mL WGA Alexa 594 in HBSS for 10 min at 37°C. The sample was washed by live cell imaging solution and assembled into a chamber using an imaging spacer filled with live cell imaging solution supplemented with 1% Prolong live antifade reagent for imaging.

8-color imaging including label-free SRS imaging. Cells were cultured on a glass coverslip in a 4-well plate. Cells were labeled with 5 μM BODIPY TR (Invitrogen, B34400) in HBSS for 10 min at 37°C. Then, 1 μM SiR700-Actin for 1 hour, 1X Tubulin Tracker Deep Red for 1 hour, 100 nM MitoTracker Green (Invitrogen, M7514) for 30 min, 2 drop/mL NucBlue (Invitrogen, R37605) for 30 min were added in the culture media at 37°C. Before imaging, cells were labeled with 5 μg/mL WGA Alexa 555 (Invitrogen, W32464) in HBSS

for 10 min at 37°C. The sample was washed by live cell imaging solution and assembled into a chamber using an imaging spacer filled with live cell imaging solution for imaging.

7-color pulse-chase imaging including metabolic imaging.   Cells were cultured on glass coverslips in a 4-well plate. 160 µM arachidonic acid-d8 (AA-d_8) (Cayman Chemical, 390010) and 80 µM palmitic acid-d_{31} (PA-d_{31}) (Wako Pure Chemical Industries, 16497) was added in the culture media for 18 hours at 37°C. Then the media was changed to DMEM supplemented with 10% FBS and 240 µM PA-d_{31}. After incubation for 0/3/6 hours, the cells were imaged. Before imaging, 1 µM SiR700-Actin for 1 hour, 200 nM MitoTracker Green for 30 min, 10 nM LysoTracker Deep Red (Invitrogen, L12492) for 30 min, 2 drop/mL NucBlue for 20 min were added in the culture media at 37°C. Finally, cells were labeled with 5 µg/mL WGA Alexa 594 in HBSS for 10 min at 37°C. All sample was washed by live cell imaging solution and assembled into a chamber using an imaging spacer filled with live cell imaging solution for imaging.

7-color time-lapse imaging including metabolic imaging.   Cells were cultured on glass coverslips in a 4-well plate. 160 µM AA-d_8 and 80 µM PA-d_{31} were added in the culture media for 21 hours at 37°C. Before imaging, 1 µM SiR700-Actin for 1 hour, 2 µM MitoTracker Green for 1 hour, 40 nM LysoTracker Deep Red for 30 min, 2 drop/mL NucBlue for 20 min were added in the culture media at 37°C. Finally, cells were labeled with 5 µg/mL WGA Alexa 594 in HBSS for 10 min at 37°C. All sample was washed by live cell imaging solution and assembled into a chamber using an imaging spacer filled with live cell imaging solution for imaging.

Tissue preparation for imaging

All procedures related to the care and treatment of animals were approved by The Keio University Institutional Animal Care and Use Committee (No. 18002-1). 4-week-old C57BL/6-Tg (CAG-EGFP) mouse (female) originally obtained from Japan SLC, Inc. was used for analysis. These mice express enhanced green fluorescent protein (EGFP) in the whole body by the introduction of a fusion gene coding EGFP under the regulation of a cytomegalovirus enhancer and chicken β-actin promoter. The mouse was anesthetized using isoflurane and perfused with 1X Phosphate-buffered saline (PBS) followed by 4% paraformaldehyde (PFA) (Nacalai Tesque, 09154-85) in PBS. After perfusion fixation, the brain was removed and post-fixed in 4% PFA in PBS at 4 oC for an additional three days. The brain was then sectioned into 100 µm-thick slices using a vibratome (Leica Microsystems, VT1200S) while submerged in PBS. The brain slices that were to be labeled were placed in a 4-well dish and washed in PBS. The 4-well plate was then placed on a plate shaker for a minute; this washing process was completed three times and used for every wash step. Next, tissue samples were permeabilized with 0.2% Tween 20 (Wako Pure Chemical Industries, 166-21115) in PBS for 15 minutes at room temperature. After permeabilization, tissue samples were washed with PBS and then blocked with 0.5% bovine serum albumin (BSA) (Wako Pure Chemical Industries, 010-25783) in PBS for 30 minutes at room temperature. After washing with PBS, tissue samples were incubated with a 1:400 dilution of 1.2 mg/mL anti-glial fibrillary acidic protein conjugated to Cy3 (abcam, 49874) in 0.5% BSA/PBS for 1 hour at room temperature wrapped in foil and placed on a plate shaker. After incubation with the antibody, tissue samples were washed with 0.5% BSA/PBS. Then, the brain slices were incubated with 1 µL of 400X Phalloidin Alexa 647 (Invitrogen, A22287) in 400 µL of 0.5% BSA/PBS for 60 minutes. During the last 20 minutes of Phalloidin incubation, one drop of NucBlue was added to the wells containing tissue samples. After staining, samples were washed a final time with 0.5% BSA/PBS and carefully assembled into a chamber using an imaging spacer filled with 1X PBS for imaging.

METHOD DETAILS
Integrated stimulated Raman and fluorescence microscope

For SRS imaging, a Ti:sapphire laser (Coherent, Mira900D) provides pump pulses at 76-MHz repetition rate. The central wavelength of the pump pulses is fixed at 843.26 nm with a spectral width of 0.15 nm for imaging the silent region (2000-2300 cm^{-1}), or fixed at 790 nm with a spectral width of 0.135 nm for imaging the C-H stretching region (2800-3100 cm^{-1}). The Stokes pulses for SRS imaging are provided by a laser system working at a repetition rate of 38 MHz. Specifically, a home-made polarization-maintaining ytterbium-doped fiber laser (YDFL) followed by a spectral broadening fiber optics generates broadband seed pulses with long-term stability (Ozeki, 2019). Then the broadband pulses are introduced into a tunable optical bandpass filter which is based on a 4-f optics including a galvanometric scanner and a diffraction grating. The narrowband pulses after spectral filtering are further amplified by a two-stage polarization-maintaining

ytterbium-doped fiber amplifier (PM-YDFA). By tuning the angle of the galvanometric scanner, the central wavelength of the YDFA output can be tuned from 1014 nm to 1046 nm, corresponding to a wavenumber range of 300 cm^{-1}, with a spectral width of ~0.35 nm (Ozeki et al., 2012; Ozeki et al., 2019). Fractions of pump light and Stokes light are extracted and launched to a two-photon absorption photodiode, the signal of which is input to a feedback circuit to control the cavity of YDFL, so that the pump laser and the Stokes laser can be sub-harmonically synchronized (Ozeki et al., 2012; Ozeki et al., 2019). The pump light and Stokes light are spatially combined by a dichroic mirror and temporally aligned by adjusting the time delay line. The transform-limited pulses (about 5-ps duration) for both pump and Stokes light enable the most efficient excitation of vibrational modes with a high spectral resolution of ~5 cm^{-1}. For fluorescence imaging, four CW lasers at wavelengths of 375/488/532/640 nm are combined by dichroic mirrors for the one-photon fluorescence excitation. They are modulated temporally in a frame-by-frame manner. The light for SRS imaging and fluorescence imaging are combined by a dichroic mirror and led to a x-y scanner which consists of a resonant galvanometric scanner operating at 8 kHz and an ordinary galvanometric scanner. The plane of the scanners is imaged onto the pupil of a water-immersion objective lens (Olympus, 60✕, N.A.=1.2). The light is focused on the specimen and the transmitted light is collected by another objective lens (Olympus, 60✕, N.A.=1.2). The transmitted pump light is filtered out and detected by a Si photodiode, the output of which is further demodulated by a lock-in amplifier to generate the SRS signal. The filters for filtering out the pump light are placed with a slightly shifted angle, so that the reflected light will be blocked by the objective mount, to avoid excess photobleaching or photodamage and also the possible crosstalk to fluorescence detection from forward CARS generation. The emitted fluorescence is separated by a multiband dichroic mirror. The fluorescence emission is spatially filtered by a pinhole to form the confocal regime and spectrally filtered to remove all the laser light. Then the fluorescence is introduced into a tunable optical bandpass filter and finally detected by a photomultiplier to generate the fluorescence signal. This tunable optical bandpass filter consists of a galvanometric scanner, a prism, a lens and a slit. By tuning the angle of the galvanometric scanner, the detected wavelength of fluorescence can be controlled. The spectral response of fluorescence detection has a flat top and sharp edges when the slit width is set as 1 mm for imaging experiments (Figure S1). At sample plane, the laser power is ~31-34 mW for SRS pump light, ~46 mW for SRS Stokes light, ~2-4 μW for 375-nm CW light, ~34-170 μW for 488-nm CW light, ~48-240 μW for 532-nm CW light, ~33-165 μW for 640-nm CW light.

Chemical mixture

Chemical mixture was prepared by mixing polyamide (PA) particles (Sigma-Aldrich, GF71024565-1EA), poly(ethyl methacrylate) (PEMA) particles (Polysciences, 03197-250), poly(methyl methacrylate) (PMMA) particles (Sekisui, SSX-110), polystyrene (PS) particles (Polysciences, 07312), Bright Blue (BB) microspheres (Polysciences, 18339), Yellow Green (YG) microspheres (Polysciences, 15700), Yellow Orange (YO) microspheres (Polysciences, 18720), and Fluoresbrite 641 microspheres (Polysciences, 21116) in distilled water (Wako Pure Chemical Industries, 049-16787).

Data acquisition and processing

The raw frames (80 ✕ 80 μm², 500 ✕ 500 pixels) with different imaging parameters were acquired at a speed of 30 frames per second for each of SRS and fluorescence channel. For the 8-color imaging of chemical mixture, imaging parameters were set as 2900 cm^{-1}, 2930 cm^{-1}, 2950 cm^{-1}, 3050 cm^{-1} for SRS channel, and as Ex375/De447, Ex488/De510, Ex532/De560, Ex640/De680 for fluorescence channel. For the 8-color organelle imaging of cells, imaging parameters were set as 2057 cm^{-1}, 2080 cm^{-1}, 2191 cm^{-1}, 2215 cm^{-1} for SRS channel, and as Ex2P/De510, Ex488/De510, Ex532/De617, Ex640/De650, Ex640/De730 for fluorescence channel. For the 8-color cell imaging including label-free SRS imaging, imaging parameters were set as 2850 cm^{-1}, 2937 cm^{-1} for SRS channel, and as Ex375/De460, Ex488/De510, Ex532/De565, Ex532/De617, Ex640/De650, Ex640/De730 for fluorescence channel. For the 7-color tissue imaging including label-free SRS imaging, imaging parameters were set as 2850 cm^{-1}, 2883 cm^{-1}, 2930 cm^{-1}, 3015 cm^{-1} for SRS channel, and as Ex375/De460, Ex488/De510, Ex532/De568, Ex640/De665 for fluorescence channel. For the 7-color cell imaging including metabolic imaging, imaging parameters were set as 2103 cm^{-1}, 2197 cm^{-1} for SRS channel, and as Ex375/De460, Ex488/De510, Ex532/De617, Ex640/De650, Ex640/De730 for fluorescence channel. The frames with the same parameters were averaged to images. The images which have crosstalk are linear-unmixed through $I = FM^{-1}$, where

$$I = \begin{bmatrix} I_{o1} & \dots & I_{on} \end{bmatrix},$$
$$F = \begin{bmatrix} F_{p1} & \dots & F_{pn} \end{bmatrix},$$

$$M = \begin{bmatrix} \sigma_{o1,\,p1} & \cdots & \sigma_{o1,\,pn} \\ \vdots & \ddots & \vdots \\ \sigma_{on,\,p1} & \cdots & \sigma_{on,\,pn} \end{bmatrix}.$$

Here, I_o is the unmixed signal intensity representing the concentration of certain probe or substance; F_p is the raw pixel value of the channel with certain imaging parameters; and $\sigma_{o,p}$ is the spectral contribution of certain probe or substance to the certain channel. The biological images were denoised: the single images were denoised by BM3D (Dabov et al., 2007b); the time-lapse images were denoised by VBM3D (Dabov et al., 2007a) (Figure S9). The nucleus, PM and artifacts were masked to generate binary images for further analysis and the depiction of contours. The images after denoising without any further processing were used for statistical analysis. To analyze the time-lapse images, pixel-wise average image was calculated representing the static information across the time-lapse stack; difference images were extracted by subtracting the average image from each image at each time point representing the dynamic information; and maximum intensity projection of the difference images was calculated. For clarity of visualizing image data related to time-lapse imaging, the tubular components of tubulin and actin were extracted using the Tubeness plugin of Fiji (Schindelin et al., 2012). To analyze the metabolic images, the images of AA/PA ratio were calculated via dividing the AA images by the PA images and additionally applying a 5 × 5 filter; and only the AA/PA ratios of the pixels which have high PA signals are shown. In the scatterplots related to AA/PA ratio, these pixels were plotted; and the signal intensity of different components in the adjacent area were the average values of 9 × 9 pixel matrices. Image contrasts were adjusted manually for clear visualization.

Calculation of relative distance to PM

The relative distance to PM was calculated according to the following equation (Figure S10):

$$Relative\ distance\ to\ PM = \frac{d_{PM}}{d_{PM} + d_{Nucleus}}$$

Here, d_{PM} is the minimum distance to PM contour; $d_{Nucleus}$ is the minimum distance to nucleus. The value outside the PM is defined as zero; the value inside the nucleus is defined as one.

Calculation of correlation coefficient

To quantify the colocalization of different organelles, the binary correlation coefficients were calculated according to the following equations:

$$r_{2o} = \frac{\sum_{i=pixel}\left(I_{o1,\,i} - I_{o1,bg}\right)\left(I_{o2,\,i} - I_{o2,\,bg}\right)}{\sqrt{\sum_{i=pixel}\left(I_{o1,\,i} - I_{o1,\,bg}\right)^2 \sum_{i=pixel}\left(I_{o2,\,i} - I_{o2,\,bg}\right)^2}}.$$

Here, r_{2o} is the binary correlation coefficient; $I_{o,i}$ is the signal intensity of each pixel inside the PM mask for certain organelle; $I_{o,bg}$ is the signal intensity of the background for certain organelle that is defined by the median of the signal intensities of pixels outside the PM mask. Compared to the conventional Pearson correlation coefficient, the average values were replaced with the background values to avoid the possible error from the biologically meaningless background.

QUANTIFICATION AND STATISTICAL ANALYSIS

Details of the statistical test are described in the main text and the figure legends. Details of the parameters used in the statistical test are described in the method details.